Ab Initio Cyclic Voltammetry on Cu(111), Cu(100) and Cu(110) in Acidic, Neutral and Alkaline Solutions

Alexander Bagger,[†] Rosa M. Arán-Ais,[‡] Joakim Halldin Stenlid,[¶] Egon Campos dos Santos,[¶,§] Logi Arnarson,[†] Kim Degn Jensen,[†] María Escudero-Escribano,[†] B. Roldan Cuenya,[‡,‖,⊥] and Jan Rossmeisl[*,†]

[†]Department of Chemistry, University of Copenhagen, Universitetsparken 5, Copenhagen, Denmark

[‡]Department of Interface Science, Fritz Haber Institute of the Max Planck Society, 14195 Berlin, Germany

[¶]Department of Physics, Stockholm University, Se-106 91 Stockholm, Sweden

[§]Departamento de Quimica, ICEx, Universidade Federal de Minas Gerais, Belo Horizonte, 31.270-901, Minas Gerais, Brazil

[‖]Department of Physics, Ruhr-University Bochum, 44780 Bochum, Germany

[⊥]Department of Physics, University of Central Florida, 32816 Orlando, USA

E-mail: jan.rossmeisl@chem.ku.dk

1

Abstract

Electrochemical reactions depend on the electrochemical interface; between the catalytic surfaces and the electrolytes. To control and advance electrochemical reactions there is a need to develop realistic simulation models of the electrochemical interface to understand the interface from an atomistic point-of-view. Here we present a method for obtaining thermodynamic realistic interface structures, a procedure to derive specific coverages and to obtain *ab initio* simulated cyclic voltammograms. As a case study, the method and procedure is applied in a matrix study of three Cu facets in three different electrolyte. The results are validated by a direct comparison with experimental cyclic voltammograms. The alkaline (NaOH) electrolyte CV are described by H^* and OH^*, while neutral ($KHCO_3$) the CO_3^* species are present and in acidic (KCl) the Cl^* species dominate. An almost one-to-one mapping is observed from simulation to experiments giving an atomistic understanding of the interface structure of the Cu facets. The strength of atomistic understanding the interface at electrolyte conditions will allow realistic investigations of electrochemical reactions in future studies.

Introduction

Electrochemical energy conversion is key for obtaining a sustainable society.[1] Despite the long and well-established history of (electro)catalysis, further understanding of the electrocatalytic interface for electrochemical reactions is needed. Computational studies within catalysis have revealed scaling relations,[2,3] and this has been used to gain fundamental insight of catalytic reactions. This has accelerated catalyst development in combination with computational screening of surfaces,[4] as the scaling relations can be used to derive *Sabatier* principles between calculated binding energies and the experimental activity of materials.[5,6] However, in these models inclusion of the electrolyte or surrounding conditions has only been sparsely investigated at the atomic-scale, but interest has increased.[7]

A particular useful experimental technique to gain an understanding of the catalyst-electrolyte interface is cyclic voltammetry (CV). CVs can be carried out on different electrode materials, however, preferable on well characterized single crystal electrodes. From CVs distinct oxidation and reduction features can be observed, which define the electrochemical properties of the electrochemical interface. Under specific experimental conditions (pH, anions, cations, scan rate *etc.*) the features in the CVs are considered to be a fingerprint of the interface. Ultimately explaining the electrochemical features observed in a CV gives an understanding of the complex electrochemical interface region.

To date, the most intensively studied single crystal system is Pt,[8–10] as Pt catalyst materials are state-of-the-art catalyst material in polymer electrolyte membrane fuel cells. Other metallic single crystal surfaces such as Ag,[11,12] Au,[8,9] Pd,[10,13] Rh,[10] Ir,[8,14] Ru[15] and Cu[16–21] have also been investigated in the literature.

The Cu single crystals are an interesting electrochemical interface to study as Cu metal has been shown to enable electrochemical CO_2 and CO reduction reactions towards valuable hydrocarbon products[22,23] and the product distribution have been shown to be dependent on both the different facets and the electrolyte.[24–28] Hence, understanding Cu single crystals in contact with different electrolytes in the metallic phase are of great interest.

In Figure 1a the *Pourbaix* diagram for Cu shows the stable phases as a function of the Standard Hydrogen Electrode (SHE) potential and pH. In this work, only the potentials and pH values where metallic Cu is stable is of interest. In Figure 1a we have colored the three pH-potential regions in which the electrochemical interface will be screened, that is; Acidic (yellow), Neutral (green) and Alkaline (blue).

Metallic Cu single crystals have been investigated previously experimentally. *E.g.* Cu(111) in alkaline NaOH conditions have been studied by CV and Scanning Tunneling Microscopy (STM) showing asymmetric double adsorption peaks around 0.05 V_{RHE} and double desorption peaks around -0.05 V_{RHE}.[16–19] For Cu(100) in NaOH CVs have been shown to be stable and symmetric adsorption and desorption peaks observed around -0.15 V_{RHE}.[16–18] However, as recently shown in a comprehensive work and literature study by *Engstfeld et. al*,[21] the Cu(100) CV peak shape, -size and -potential depends on both preparation procedure and amount of residual O_2 in the electrolyte. Clearly, this introduces several uncertainties for the interpretation of the Cu CVs. For Cu(110) in NaOH a relatively flat CV has been observed.[18]

In the intermediate (neutral) pH range, single crystal CVs on Cu(111) and Cu(100) have been measured in a CO(g) saturated phosphate buffer.[28] These experiments show adsorption and desorption peaks for Cu(100) around -0.3 V_{RHE}, in good agreement with our recent calculations on Cu(100) with CO and phosphate species.[25]

In the acidic region, CVs have been measured for Cu(111), Cu(100) and Cu(110) in $HClO_4$ showing featureless/flat CVs.[20] Below the typical CV potential region of Cu, in the HER region, reconstruction of the Cu(100) facet has been observed by STM.[29] Adding HCl to the $HClO_4$ electrolyte or using HCl electrolyte changes the Cu(111) and Cu(100) CV from featureless to having broad adsorption and desorption features at low potentials.[30–32]

Herein we study the Cu(111), Cu(100) and Cu(110) facets by *Ab Initio* Molecular Dynamics (AIMD)[34,35] simulations of explicit electrolytes in contact with the surfaces. From these, we obtain energies as a function of the workfunction. This can be linked to the potential and ionic strength dependence by employing the Generalized Computational Hydrogen
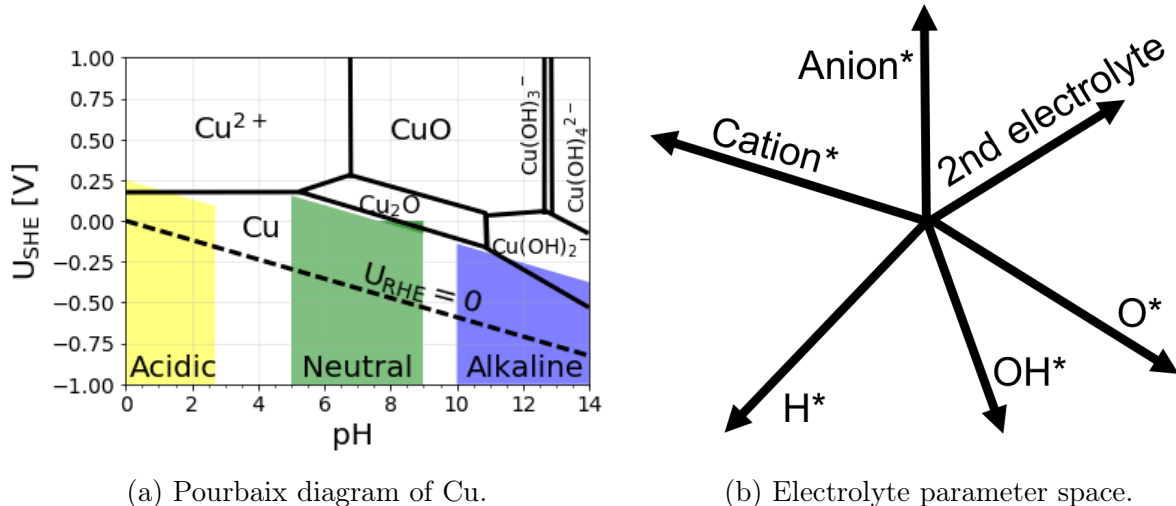
(a) Pourbaix diagram of Cu. (b) Electrolyte parameter space.

Figure 1: (a) Pourbaix diagram of Cu with the different stable phases as a function of potential (U_{SHE}) and pH at 25°C. Regions of Cu(s) covered by cyclic voltammetry are marked as Acidic (yellow), Neutral (green) and Alkaline (blue). Dashed line show U_{RHE}=0 V, with a slope of -0.059 V/pH. Data is adapted from.[33] (b) Show the electrolyte parameter space when investigating electrolytes in contact with a metal facet. The parameters, H*, OH*, O*, Cation*, Anion* and 2nd electrolyte properties can all give a response in the experimental measured CV. The 2nd electrolyte corresponds to mixing multiple anions and cations.

Electrode (GCHE),[25,36,37] as a posterior analysis of the system. This scheme allows explicit calculation of interface phase diagrams, allows to derive the coverage of species and calculation of theoretical CVs for a set of surface structures. The theoretical CVs are then compared directly to experimental CVs and when features allow it, a fitting procedure from experiment to calculated states is carried out. It should be noted that computational CVs are a less studied field, due to the difficulties of simulating the electrochemical interface, as compared to binding energy and trend studies. Whereas, calculation of adsorbate coverages can be found in literature.[37–40]

Investigation the three Cu facets with three pH/electrolyte regions entails a massive number of parameters to be simulated/screened. This parameter space is shown in Figure 1b, with coverages of H*, OH*, O*, Cation, Anion and 2nd electrolyte parameters that in principle require calculations and further their combinations. *E.g.* as a minimum, only considering H* and OH* states and their combinations up to half monolayer (ML) coverage

in a 12 atom unit-cell requires $7 \times 7 = 49$ AIMD simulations. Including Cation, Anion and 2nd electrolyte show that it is impossible to span the whole parameter space. One has to be selective with respect to resources and iteratively select relevant electrolyte parameters to simulate.

The work uses a method that gives an interface in equilibrium with the electrochemical conditions, and ideally, this should correspond to the experimental CV profiles. However, the modeling does have its limitations and assumptions, which are listed below:

- No reconstruction of the Cu(*hkl*) facet is considered.
- The simulated CV only include structures/adsorbates which are selected with respect to the electrolyte (*i.e.* no impurities).
- The simulated CV corresponds to a reversible CV scan. Here the comparison is carried out with respect to the anodic scans.
- The simulated CV and available coverages are limited by the finite unit-cell.
- Only some configurations (naturally occuring in the AIMD) is considered in the simulations.
- Estimating the adsorbates entropy in the interface with respect to the electrolyte is difficult.

Finally, it is important to realize that the peak positions of the simulated CV per default will rely mainly on absolute values and only marginally on trend schemes, which is typically the strength of the successful volcano and scaling relation based Density Functional Theory (DFT) studies.[2,3] However, as we do carry out an experimental and simulation type of matrix study between Cu facets and electrolytes shown in Table 1, this mapping allows us to cross-reference our absolute values and hence make our conclusions more robust.

Table 1: Experimental and simulation matrix investigation of the three Cu facets in three different electrolyte and pH conditions under Ar saturation. Top row for the facets shows the electrolyte conditions while lower row shows the included simulated surface adsorbates.

	Acidic (pH~1)	Neutral (pH~8.3)	Alkaline (pH~13)
Cu(111)	0.1M $HClO_4$ + 0.01M KCl	0.1M $KHCO_3$	0.1M NaOH
	H^*, OH^*, Cl^*	H^*, OH^*, HCO_3^*, CO_3^*	H^*, OH^*
Cu(100)	0.1M $HClO_4$ + 0.01M KCl	0.1M $KHCO_3$	0.1M NaOH
	H^*, OH^*, Cl^*	H^*, OH^*, HCO_3^*, CO_3^*	H^*, OH^*
Cu(110)	0.1M $HClO_4$ + 0.01M KCl	0.1M $KHCO_3$	0.1M NaOH
	H^*, OH^*, Cl^*	H^*, OH^*, HCO_3^*, CO_3^*	H^*, OH^*

Methodology and Results

The procedure to make *ab initio* cyclic voltammograms is explained here followed by simulations and experiments of Cu(hkl) in alkaline, neutral and acid media. The procedure is shown in Figure 2, which has been divided into five steps:

(1) Relevant simulations of electrolyte structures are performed. For aqueous electrolytes this comprises of the clean water-covered surface, H*, OH*, potentially also O*, cations, anions and other electrolyte species/intermediates.

(2) The chemical potential is set for all species with respect to electrolyte conditions, accounting for pH and concentrations.

(3) The *Boltzmann* weight is carried out to give a distribution with the most stable configurations. It can be carried out both in terms of the energy or coverage, as shown in the left and right at step (3) of Figure 2.

(4) The slope of the Boltzmann weighted energy corresponds to the charge in the interface. Differentiating the Boltzmann weighted energetics one obtain the isotherm from the surface.

(5) Differentiating one more time and multiplying with a chosen scan rate gives a simulated CV.
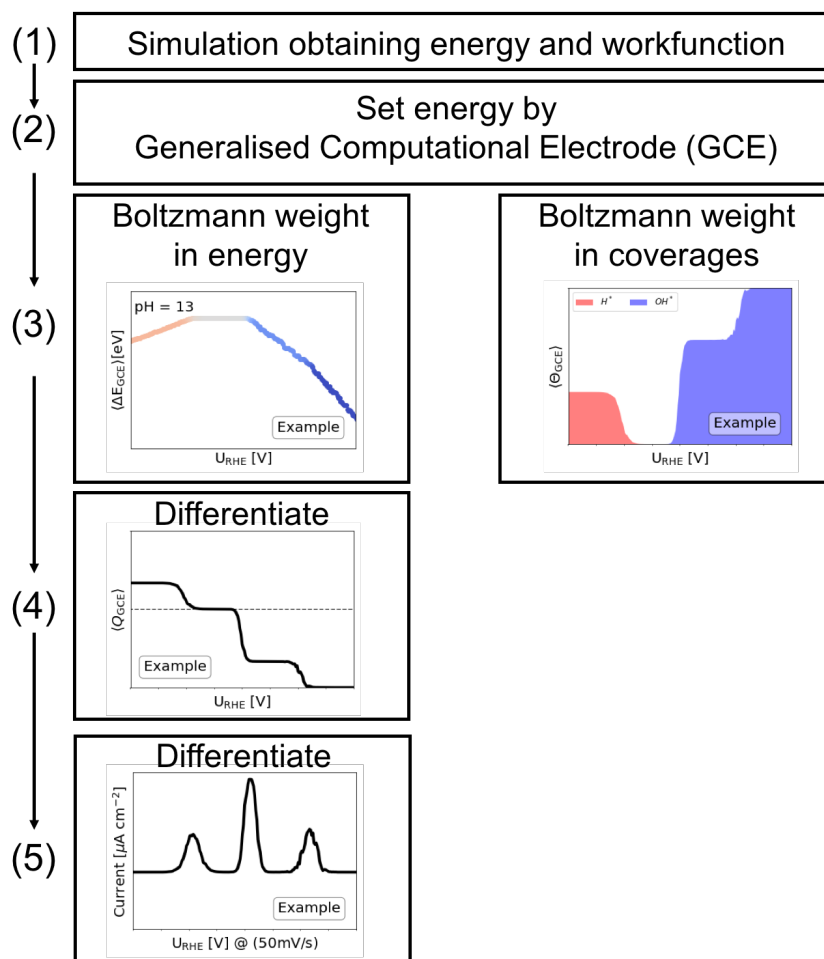
Figure 2: Flow diagram showing the layout of how to obtain coverages and CVs of an interface model. The method consists of five steps (1) calculation of structures with energetics and workfunction, (2) setting the energetics correct with respect to the electrolyte far away from the electrode, (3) carry out the Boltzmann weighting to obtain the most stable configurations either in terms of energy or coverage, (4) differentiating the energetics to obtains the phase isotherms while (5) differentiating one more time and multiplying by a scan-speed to obtain the relevant CV.

Alkaline

The first simulations needed to create the corresponding theoretical CVs requires simulation of the different coverages of H* and OH*. This set of simulation can represent CVs where cation and anions have a minor influence. Specifically for the Cu system, we have previously showed that the binding energies are almost unaffected by cations present.[25] Hence, for the three Cu facets in alkaline (NaOH) these simulations are carried out and the stepwise procedure shown in Figure 2 is used. From this, the coverages and simulated CVs are obtained as shown in Figure 3 top and middle row.

Experimental CVs in NaOH is shown in the lower row of Figure 3. The Cu(111) facet is observed to have a double peak, the Cu(100) has one symmetric peak and the Cu(110) is rather featureless. This is similar to the experiments by *Schouten et al.*[18] Interpretation of the experimental CVs is to integrate the CV peaks as shown in Figure S1 for relevant anodic scans. Figure S1a reveals that the Cu(111) double peak corresponds roughly to about 3/12 or 4/12 ML charge. Figure S1b show that the broad Cu(100) peak corresponds to 4/12 ML charge. For the case of Cu(111) and Cu(100) the experimental features allow for a fitting of the simulated states, and this illustrates the deviation of the OH* adsorption onset potential from simulations to experiment.

The Cu(111) simulation in Figure 3 shows coverage of 0.33 ML (4/12 ML) OH*, which is similar to the experimental integrated double peak. However, the peak has an earlier potential onset than the experimental results and the fit primarily move the OH* towards weaker binding.

The Cu(100) simulation in Figure 3 also reveals a coverage of 0.33 ML (4/12 ML) OH*, which is similar to the integration of the experimental peak. However, again the OH* binds too strong relative to experiments and by fitting the rising OH* coverage at more positive potential resemble the experiment.

The OH* shift for Cu(111) is roughly 0.1 eV destabilization pr. OH*, while for Cu(100) including only H* and OH* states the destabilization is larger (see Table S6). Another

possibility for the experimental CV for Cu(100), is that combinations of H* and OH* are present. In Figure S6 the result with combinations are shown and the fitting parameters are given in Table S8. This shows close to similar destabilization energy per. OH* with Cu(111). Furthermore, it illustrates that multiple solutions to such experimental CVs exist and knowing the exact potentials and coverages are difficult.

The Cu(110) simulation exhibits a fixed OH coverage of 0.18 ML (3/16 ML) OH* over the investigated potential range, which resembles the flat experimental CV *i.e.* no fitting is carried out.

Including only simulated H* and OH* intermediates in the interface to calculate theoretical CVs is shown to give a relatively good fit for the alkaline CVs of the Cu facets. Minor offset in simulated and experimental peak positions are observed, which can be a result of deviating absolute DFT values. Simulating alkaline Cu CVs by only H* and OH* is slightly different from the usual interpretation of Pt single crystal CVs, which is commented in the later discussion.
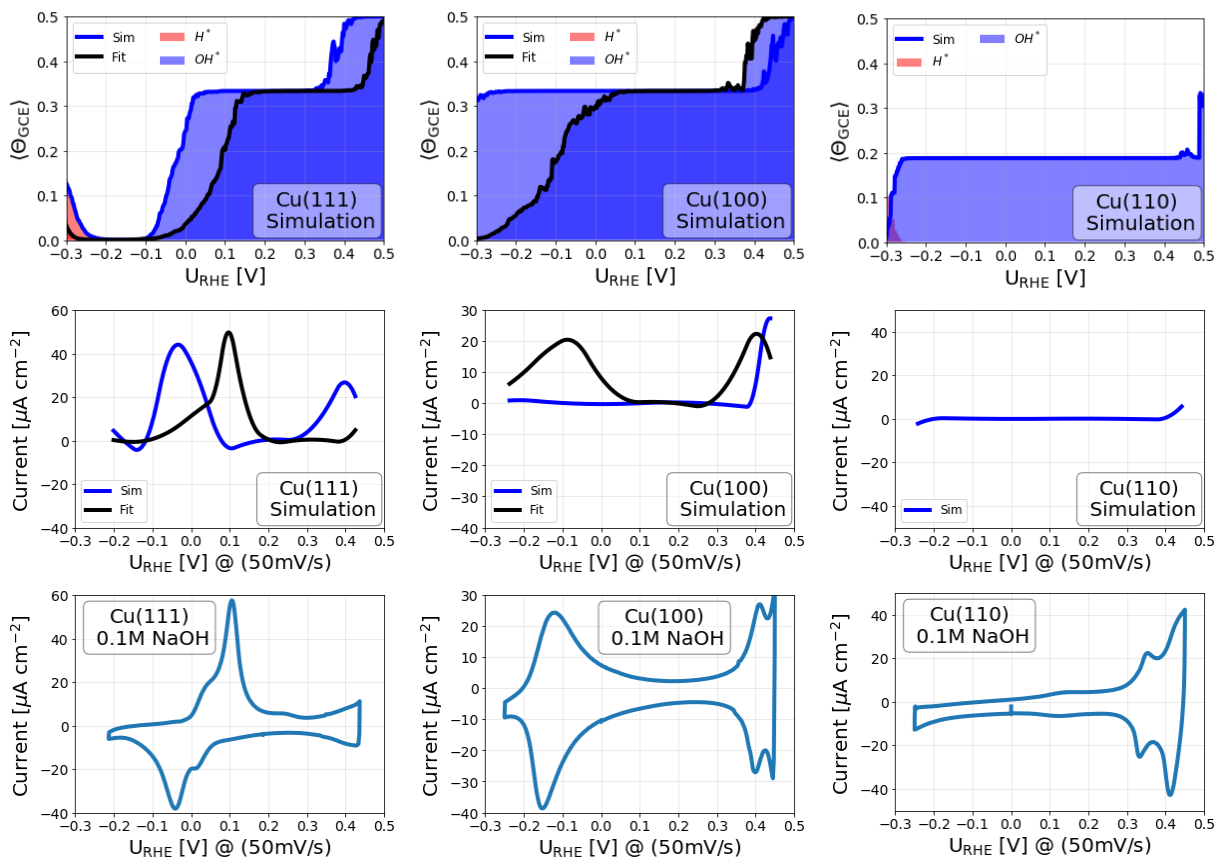
Figure 3: Simulations and fitting of H* and OH* coverages, the derived CVs and the experimental CVs in alkaline (NaOH) for the three Cu(hkl) facets. The experimental Cu(111) has a double peak and the Cu(100) has a broader single peak, which after fitting reveal that the absolute values of the simulated OH* have an energy offset. The experimental Cu(110) is rather flat and featureless, which simulations replicate nicely. At high overpotential, close to the oxidation potential, the features can originate from O* adsorption. Fitting parameters are given in Table S6.

Neutral

For neutral electrolytes, different cation and anion configurations could be considered. Previously we have shown simulated results for phosphate and carbonate anions on the Cu(100) facet[25] and CO_3^* has been experimentally observed on polycrystaline Cu in $KHCO_3$.[41]

In Figure 4 simulations and fits consider bicarbonate anions as-well as H^* and OH^* together with the experimental CVs in $KHCO_3$ for the three Cu facets. The features of the experimental CVs change significantly with respect to the alkaline NaOH CVs shown in Figure 3.

Experimentally the Cu(111) CV anodic scan exhibits two separate peaks and one cathodic peak. The difference in anodic and cathodic scan led to speculation of reconstruction on the Cu(111) facet,[42] which is not addressed here. Integrating these two peaks indicate that the first peak corresponds to 2/12 ML charge and the smaller second peak increases the charge coverage to 3/12 ML, see Figure S1c. The experiment for Cu(100) have a small decrease of charge over the potential range investigated and the Cu(110) experiment exhibits a minor increase in charge due to a subtle feature around -0.05 V_{RHE}.

For the bicarbonate CV at Cu(111), the found corrections for the alkaline Cu(111) CV is used for H^* and OH^* together with simulations of HCO_3^* and CO_3^* anions. Here the coverage of a CO_3^* anion is set to 2/12 ML to match the charge and the fact that the anion approximately takes up two sites at the surface. This shows that initially one CO_3^* anion and an OH^* adsorps and later the CO_3^* coverage increase. This results in two relatively sharp peaks with two much charge as compared to the experiment. When fitting is carried out the CO_3^*, $2CO_3^*$ and $1OH^*$ states are all destabilized allowing for a better fit to experiment. Although within reasonably values as listed in Table S7. Another potential strong binding solution for CO_3^* anions can also be found, and is shown in Figure S7, with the fitting values in Table S9. Finally a pure OH^* and H^* solution could also be made, but is neglected due to the observation of CO_3^* on polycrystaline Cu.[41]

The Cu(100) simulation shows a surface covered by two CO_3^* anions giving rise to a

relatively featureless CV comparable to the experiment. Only a smaller tail decaying moving from low potential to higher potential originate from early adsorption of the carbonate anions.

The Cu(110) simulation shows first a 3/16 ML OH* coverage (blue) and followed by two CO_3^* anions adsorbed (green). This gives rise to a peak in the simulated CV, whereas the experimental CV is flatter. The fitted model suggests that CO_3^* also binds stronger relative to that indicated by the experiment.

It is observe that adding carbonate anion species to the simulations agrees relatively well with the experimental CVs. The dual peak of Cu(111) is almost reproduced, the featureless Cu(100) CV arise due to a constant CO_3^* coverage and the Cu(110) deviate a bit.
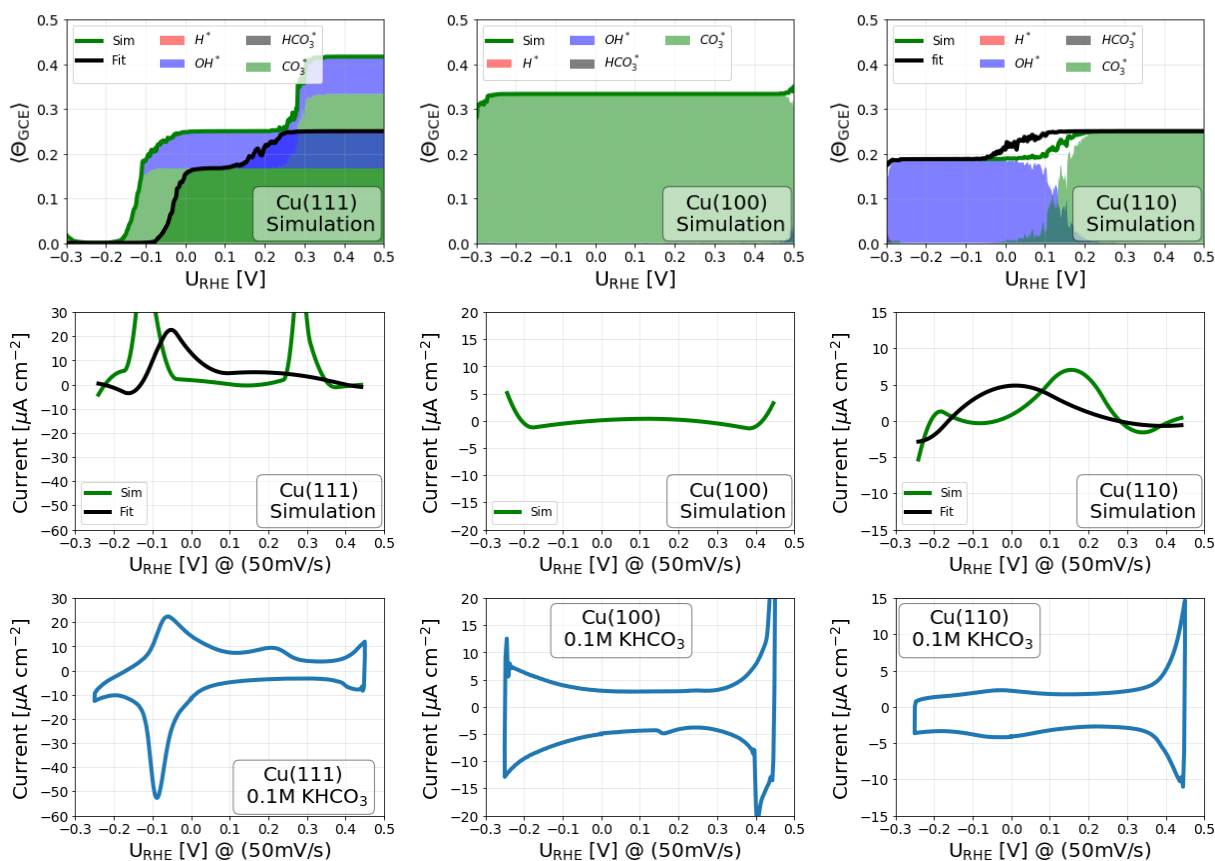
Figure 4: Simulations and fitting of H*, OH*, HCO_3^* and CO_3^* coverages, the derived CVs and the experimental CVs in neutral (KHCO$_3$) for the three Cu facets. Each CO_3^* has been set to cover two surface sites. For these simulations the carbonate, CO_3^*, bind strongly to the surface through the oxygen and hence poisoning the surface with respect to the OH* intermediates in all three cases, representing the experimental CVs well. Fitting parameters for Cu(111) is given in Table S7.

Acidic

For the acidic electrolyte, we investigate the influence of the strong adsorbing Cl* species for the Cu facet CVs.[39] The previous investigations showed that the strong adsorbing Cl* anions can give rise to adsorption/desorption features at low overpotential[30–32] and importantly the Cu surface is known to reconstruct in acidic conditions.[29]

In this work, the experimental CVs for $HClO_4$+KCl electrolytes for Cu(111) and Cu(100) in both cases reveal featureless CVs, as shown in Figure 5. While for the Cu(110) an almost symmetric peak is observed at -0.1 V_{RHE}, corresponding to a change in charge of 1/16 ML, as integrated in Figure S1d.

The Cu(111) simulations show an initial coverage of 1/12 ML Cl* and an increase up to 3/12 ML Cl* at -0.1 V_{RHE}. This increase gives rise to a broad region of positive current in the simulated CV. Compared to our experimental Cu(111) $HClO_4$+KCl CV, this broad feature is not existing. Instead, an increased negative current is observed from slow HER while having Cl* at the surface.

The Cu(100) simulations show a constant coverage of 3/12 ML Cl* in the investigated region. This results in a flat featureless simulated CV, which is identical to the experiment. At higher potentials, the simulation shows higher Cl* coverage, while the experimental CV show oxidation/dissolution.

The Cu(110) simulations show an initial Cl* coverage of 3/16 ML which increases to 4/16 ML Cl* giving rise to a simulated peak in the CV. This change in charge corresponds to the experimental CV, where the charge at the surface is increased at -0.1 V_{RHE}. The fitted simulations show that only minor binding energy changes of Cl* move the simulated peak to fit the experiment. Note that this can also be a result of reconstruction at the surface by the strong Cl* interaction.
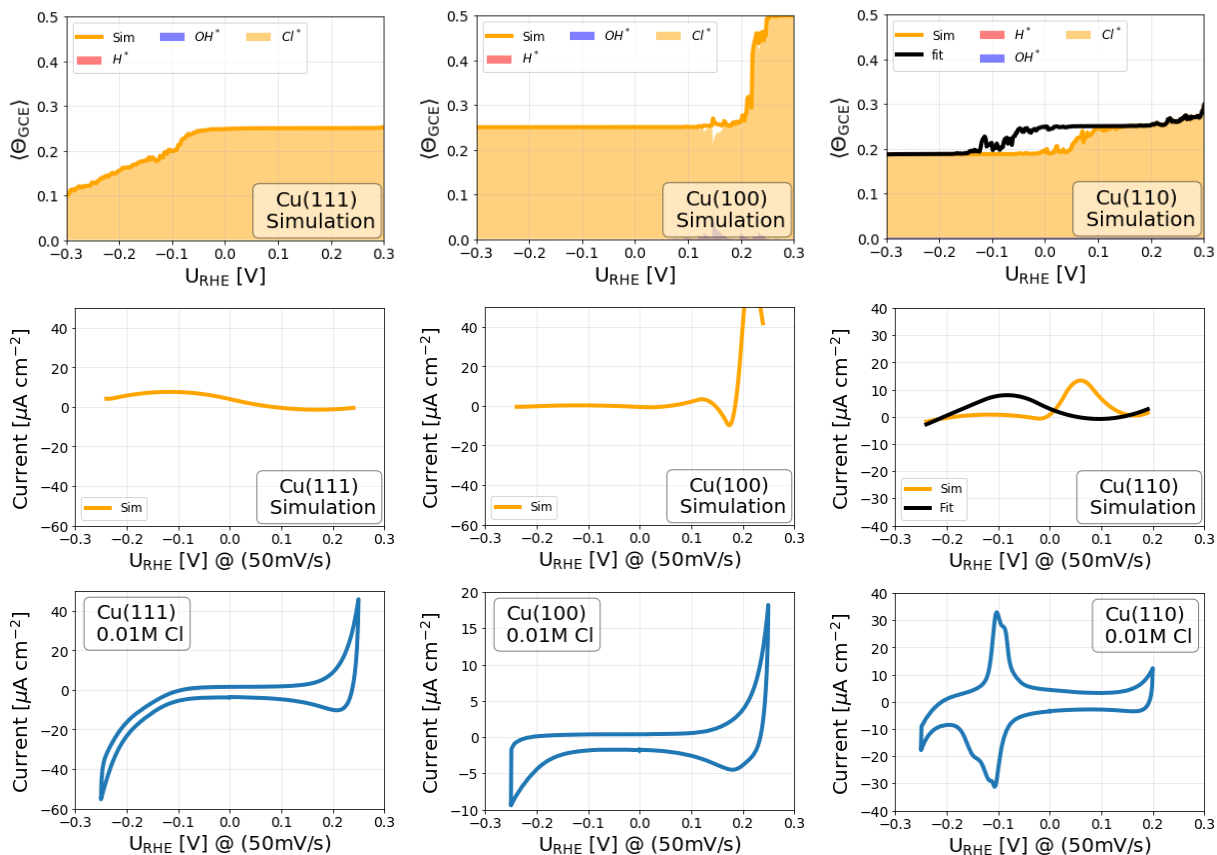
Figure 5: Simulations and fitting of H*, OH* and Cl* coverages, the derived CV and the experimental CV in acidic (HClO$_4$ + KCl) for the three Cu facets. The Cl anion, known to poison surfaces, bind strongly to the surface and has a poisoning effect with respect to OH*, which resemble the experiments.

Discussion

This work demonstrate how it is possible to utilize AIMD simulations of explicit electrolytes in contact with various surface facets to calculate coverage of H*, OH* and different anions. Further, CVs have been derived and compared to experiments. A relatively good comparison is shown, and by fitting the simulations, the origin of the differences are shown clearer. However, it is highly relevant to discuss (i) the differences between AIMD and vacuum simulations, (ii) is the workfunction reference needed and (iii) differences between proposed inactive $HClO_4$ and $NaOH$ electrolytes.

(i) Is the AIMD, calculating the energy and workfunction to utilise the GCE scheme is really needed to obtain valid coverages on an RHE scale? In Figures S2, S3 and S4 the Computational Hydrogen Electrode (CHE)[2] surface Pourbaix diagrams and coverages are presented to be compared with the GCE result. For the H*, OH* and to some extend Cl* the AIMD GCE and CHE results are relatively close to each other, while the HCO_3^* and CO_3^* anions exhibit significant differences. To investigate if this is solely an effect of the AIMD water, the energies of H*, H_2O, Cl*, CO*, HCO_3^* and CO_3^* are shown by ΔE_{AIMD} vs. ΔE_{vacuum} in Figure 6. The figure elucidates that H*, Cl* and CO* energetics are obtained similar in AIMD and vacuum, with minor differences of H_2O, while CO_3^* is very different with an around 2.5 eV difference in binding energy. This could be a result of the references used to set the energy of CO_3^*, by the following equation:

$$CO + 2H_2O \rightarrow CO_3^* + 2H_2.$$
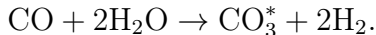
However, the references CO→CO*, H_2O(g)→H_2O and $\frac{1}{2}H_2 \rightarrow$ H* show that the strong binding of CO_3^* is mainly a result of the AIMD water stabilisation. This shows that some intermediates/anions need the explicit water stabilization, which is in agreement with our previous work.[25]

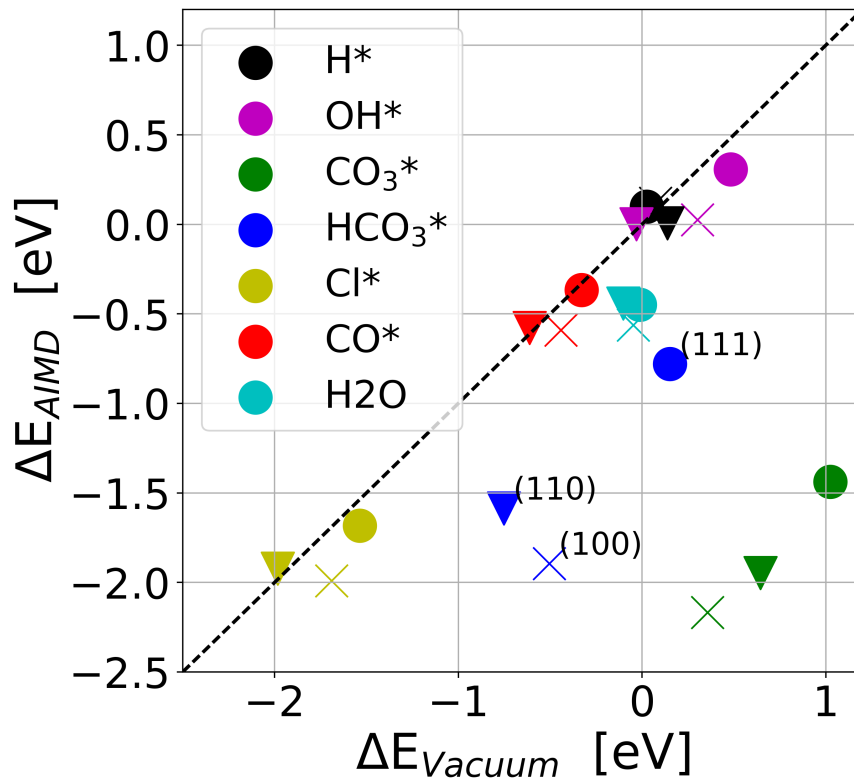(ii) One could speculate whether it is necessary to calculate the workfunction and utilize

Figure 6: Comparison of binding energies between aqueous electrolyte AIMD simulations and vacuum simulation for single adsorbates. For both types of calculation the same references are used. Colors determine the adsorbate and marker the Cu facet.

this as a second reference point. The GCE scheme use the workfunction to get structures at the right potentials. This is important for cases where the specific structure of the interface at a potential is needed. Furhter, for coverages and CVs, if the energetics are close to each other (in the order of $\sim k_B T$). While if the energetics of two comparable states are larger than $k_B T$, then the energetics dominate and the sampling of the workfunction is negligible for the purpose of CV and coverage plots.

(*iii*) Interestingly the H* and OH* simulations seem to fit the alkaline CV for Cu, as compared to Pt CV interpretations. For Pt, the H* and OH* simulations have been suggested to fit the acidic CVs in the proposed inactive $HClO_4$ electrolyte.[40] However, there are differences between Cu and Pt. The workfunctions are $5.12 - 5.93$ eV and $4.53 - 5.10$ eV for Pt and Cu, respectively. Furthermore, the binding energies are different and the potential region of the CVs.

18

A comparison of the HClO$_4$ and NaOH electrolyte experiments is shown in Figure 7 for Cu(111) and Cu(100) on RHE scale. The HClO$_4$ experiments show features close to the ionisation potential of Cu→Cu^{2+}. The simulation of ClO$_4^*$ anion would be preferable to simulate the CV. However, trying to carry out the ClO$_4^*$ anion calculation in the AIMD model reveal that interface potential is below the stable ClO$_4^*$ ion potential and the ion quickly breaks apart into other ions. Whether Cu surfaces really reduces the ClO$_4^-$ ion to obtain a small ClO$_x$ coverage is not known. Here simulating H* and OH* in equilibrium at pH $= 1$ show that this does not corresponds to the HClO$_4$ electrolyte CVs. In that instance simulations rather exhibits the peak features seen in the NaOH CVs. But retroactively comparing the NaOH and HClO$_4$ CVs does reveal similarities in the CVs. The Cu(111) HClO$_4$ has some asymmetric peak at a higher RHE potential than NaOH which also has an asymmetric peak. The Cu(100) HClO$_4$ has a smaller symmetric peak at higher potential than the NaOH symmetric peak. Hence, the HClO$_4$ CVs could probably be fitted by only the H* and OH* although by at big destabilisation of the OH* as compare to the NaOH case. This could indicate a plausible solution of ClO$_x$ species covering the surface, and a certain potential is required for OH* to displace those and increase the coverage, leaving a similar, but smaller OH* feature at higher potential. However, this puzzle remains unsolved.
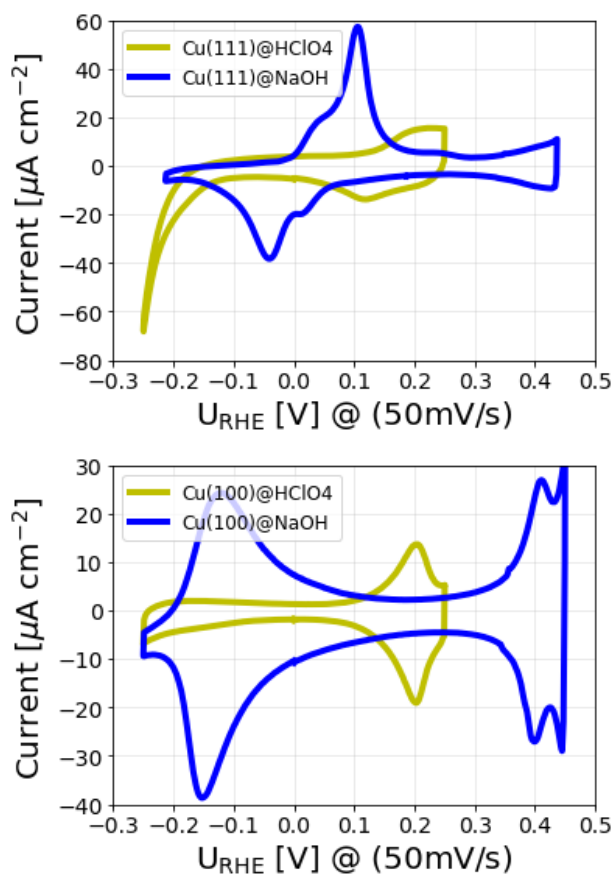
Figure 7: CV experiments of Cu(111) and Cu(100) in HClO$_4$ (acidic) and NaOH (alkaline) electrolytes. The two facets in the two electrolytes have similarities; Cu(111) peaks are asymmetric and Cu(100) peaks are symmetric. However, for both facets, the features in HClO$_4$ are at higher potential and smaller in size than in NaOH.

Conclusion

In conclusion, it has been shown that the method can be used to derive coverages and CVs from interface phase diagrams, which can be directly compared to experimental CVs. The results showed a good comparison between calculated CVs at different electrolytes and pH conditions for the Cu(111), Cu(100) and Cu(110) facet. In alkaline condition, the experiments were well described by having OH^* on the surface, while in neutral bicarbonate conditions the surfaces for the Cu facets are covered by CO_3^* anions. It is noted correct evaluation of anion adsorption in neutral pH widely relies on AIMD simulation while only a small effect on H and OH adsorption is noted relative to vacuum calculations. In acidic chloride containing media, the Cu surfaces exhibit significant Cl^* coverages. Differences between the simulations and experimental CVs were also observed. Here these deviations were fitted when possible, and it should be noted that the deviations could also be a consequence of the limitations and assumptions listed in the introduction.

The goal of being able to say something about what is on or inside the electrochemical interface is presented here, and it shows that the method can obtain realistic electrochemical interfaces. Once having realistic electrochemical interfaces, electrochemical reactions can be studied more realistic by considering the interface conditions that influence multiple reactions at acidic, neutral or alkaline conditions.

Methods

Electrochemical measurements

Prior to each experiment, Cu single crystal electrodes (MaTeck, 1 cm diameter, 99.999 %) with (100), (111) and (110) orientation were electropolished at 3 V *vs.* Ti foil for 10 s in a H_3PO_4/H_2SO_4 solution consisting of 130 mL H_3PO_4 (VWR, 85 wt%), 20 mL H_2SO_4 (VWR, 95%) and 60 mL ultrapure water (Elga, 18.2 MΩ cm). The electrodes were then rinsed with ultrapure water and quickly transferred into the electrochemical cell. Cyclic voltammetry measurements were carried out at 50 mV/s in Ar-saturated (Air Liquide, N50) solutions containing 0.1 M NaOH (ACS. Reag. Merck), 0.1 M $KHCO_3$ (99.9%, Sigma-Aldrich), and 0.1 M $HClO_4$ + 0.01 M KCl (ACS. Reag. Merck). A custom-made electrochemical cell was used in a three electrode configuration, with a gold wire as a counter electrode and a reversible hydrogen electrode (RHE, HydroFlex, Gaskatel) as a reference electrode. A BioLogic 240 potentiostat was employed to control the electrode potential.

Generalized Computational Electrode (GCE)

In order to generate the interface diagrams from our AIMD trajectories containing energy and workfunction, we apply the Generalized Computational Hydrogen Electrode scheme.[36,37]

The GCE[25] equation for different electrolyte investigations defines the energy of each state of the AIMD configurations for a given potential, concentration and pH as:

$$\Delta E_{\text{GCE}}(n, x, \phi_{e^-}, \text{pH}) = E(n, x, \phi_{e^-}) - \langle E(\{x, p\} = 0) \rangle - x\mu_{X_{(g)}}$$
$$- n\frac{1}{2}\mu_{H_2}^0 - n\overbrace{(\phi_{\text{SHE}} - \phi_{e^-} - 2.3k_BT \times \text{pH})}^{eU_{RHE}}, \text{ where } n = \{-6, .., 6\}. \tag{1}$$

Here the energy, ΔE_{GCE}, is a function of the number of protons n removed or added, the workfunction ϕ_{e^-}, pH (U_{RHE}) and the number x of adsorbates X added at thermodynamic

equilibrium conditions. μ denotes the chemical potential of a chemical species, ϕ_{SHE} is the defined standard hydrogen electrode potential of 4.4 V on the absolute scale,[44] k_B is Boltzmann's constant, T is the absolute temperature and $\langle E(\{n,x\}=0)\rangle$ is the reference energy.

However, in order to obtain the energy and coverage of the interface at specific conditions determined by eq. (1), all the GCE energy states are Boltzmann-weighted by binning the data within a bin of chosen size as:

$$\langle A \rangle = \frac{1}{Z} \sum_{i=1}^{N} A_i \exp\left(\frac{-\Delta E_{\text{GCE}}(n,p,q,\phi_{\text{e}^-},\text{pH})_i}{k_B T} \right), \quad A = \{\Delta E_{\text{GCE}}, \Theta_{\text{GCE}}\}, \tag{2}$$

where Z is the partition function, N is the total number of states in the bin and $\langle A \rangle$ is the property of interest, in this case, the energy $\langle \Delta E_{\text{GCE}} \rangle$ and the coverage $\langle \Theta_{\text{GCE}} \rangle$.

Finally, the CV current is calculated as:

$$I = \frac{dQ}{dt} = \frac{dQ}{dV} \times \frac{dV}{dt} = \frac{dE}{dV} \times \frac{1}{dV} \times \frac{dV}{dt} = \frac{dE}{dV} \times \frac{1}{dV} \times \frac{dV}{dt} \times Q_{\text{1ML}} \tag{3}$$

Where the $\frac{dE}{dV} \times \frac{1}{dV}$ is the double differentiating of the phase diagram, $\frac{dV}{dt}$ is the CV scan speed (here 50 mV/s) and Q_{1ML} is the charge of one monolayer of the three facets. Here the charge of $283 \mu C/cm^2$, $245 \mu C/cm^2$ and $347 \mu C/cm^2$ is used for Cu(111), Cu(100) and Cu(110), respectively. Carrying out the double differentiation on the Boltzmann weighted GCE states imposes considerable noise on the results, so for smoothness, the SciPy's built-in splines differentiation is used to create the CVs.

Computational details

Atomic structures were built with ASE.[45] The water interface models are constructed as orthogonal $(3 \times 4 \times 3)$, $(3 \times 4 \times 3)$ and $(2 \times 4 \times 3)$ unit cells for the (111), (100) and (110) copper facets, respectively, to obtain similar xy plane interfacial areas of the unit cells. Each water interface model consists of three water layers with a total of 24 H_2O molecules, which

are allowed to move freely during the simulation. An additional hexagonal water layer on top of the mobile aqueous phase is also kept fixed in order to keep the water density of the interface model constant and close to that of pure water. When atoms (protons or intermediates) are added and subtracted, the top water layer remains unchanged. Finally, the vacuum metal facet structures where created by removing the water layers from the water interface model.

The electronic structure calculations are carried out at the Generalized Gradient Approximation Density Functional Theory (GGA-DFT) level with the projector-augmented wave method as implemented in GPAW.[46] Different levels of electronic structure calculation were employed: (1) Finite-difference calculations are carried out for vacuum binding energies using $(4 \times 4 \times 1)$ k-points, the RPBE[47] functional and a 0.18Å grid spacing. (2) The water/copper interface is modeled by AIMD at a constant temperature of 300 K (using *Berendsen*[48] NVT dynamics, with a timestep of 0.5 fs and a time temperature cooling constant of 100 fs) as implemented in GPAW. To achieve thermal equilibration and a sufficient number of states for the GCE approach, the electronic structure calculations are carried out by RPBE[47] calculations in LCAO mode with a grid spacing of 0.18Å at the gamma point.

Acknowledgment

Competing interests

The authors declare no competing financial interest.

Keywords

Cyclic Voltammetry, Electrochemistry, Electrochemical interface models, Ab Initio Molecular Dynamics.

References

(1) Badwal, S. P. S.; Giddey, S. S.; Munnings, C.; Bhatt, A. I.; Hollenkamp, A. F. *Frontiers in Chemistry* **2014**, *2*, 79.

(2) Fernández, E.; Moses, P.; Toftelund, A.; Hansen, H.; Martínez, J.; Abild-Pedersen, F.; Kleis, J.; Hinnemann, B.; Rossmeisl, J.; Bligaard, T.; Nørskov, J. *Angewandte Chemie International Edition* **2008**, *47*, 4683–4686.

(3) Calle-Vallejo, F.; Loffreda, D.; Koper, M. T. M.; Sautet, P. *Nature Chemistry* **2015**, *7*, 403.

(4) Nørskov, J. K.; Bligaard, T.; Rossmeisl, J.; Christensen, C. H. *Nature Chemistry* **2009**, *1*, 37.

(5) Nørskov, J. K.; Bligaard, T.; Logadottir, A.; Kitchin, J. R.; Chen, J. G.; Pandelov, S.; Stimming, U. *Journal of The Electrochemical Society* **2005**, *152*, J23–J26.

(6) Man, I. C.; Su, H.-Y.; Calle-Vallejo, F.; Hansen, H. A.; Martínez, J. I.; Inoglu, N. G.; Kitchin, J.; Jaramillo, T. F.; Nørskov, J. K.; Rossmeisl, J. *ChemCatChem* **2011**, *3*, 1159–1165.

(7) Magnussen, O. M.; Groß, A. *Journal of the American Chemical Society* **0**, *0*, null.

(8) Lopes, P. P.; Strmcnik, D.; Jirkovsky, J. S.; Connell, J. G.; Stamenkovic, V.; Markovic, N. *Catalysis Today* **2016**, *262*, 41 – 47, Electrocatalysis.

(9) Schmidt, T.; Stamenkovic, V.; Arenz, M.; Markovic, N.; Ross, P. *Electrochimica Acta* **2002**, *47*, 3765 – 3776.

(10) Sashikata, K.; Furuya, N.; Itaya, K. *Journal of Vacuum Science & Technology B: Microelectronics and Nanometer Structures Processing, Measurement, and Phenomena* **1991**, *9*, 457–464.

(11) Marinković, N.; Marinković, J.; Adžić, R. *Journal of Electroanalytical Chemistry* **1999**, *467*, 291 – 298.

(12) Jovic, B.; Jovic, V.; Stafford, G. *Electrochemistry Communications* **1999**, *1*, 247 – 251.

(13) Kibler, L. A.; El-Aziz, A. M.; Hoyer, R.; Kolb, D. M. *Angewandte Chemie International Edition* **2005**, *44*, 2080–2084.

(14) Ganassin, A.; Sebastián, P.; Climent, V.; Schuhmann, W.; Bandarenka, A. S.; Feliu, J. *Scientific Reports* **2017**, *7*.

(15) Brankovic, S.; Marinkovic, N.; Wang, J.; Adžić, R. *Journal of Electroanalytical Chemistry* **2002**, *532*, 57 – 66.

(16) Jović, V.; Jović, B. *Journal of Electroanalytical Chemistry* **2003**, *541*, 13 – 21.

(17) Jović, V.; Jović, B. *Journal of the Serbian Chemical Society* **2002**, *531*.

(18) Schouten, K. J. P.; Gallent, E. P.; Koper, M. T. *Journal of Electroanalytical Chemistry* **2013**, *699*, 6 – 9.

(19) Maurice, V.; Strehblow, H.-H.; Marcus, P. *Surface Science* **2000**, *458*, 185 – 194.

(20) łLukomska, A.; Sobkowski, J. *Journal of Electroanalytical Chemistry* **2004**, *567*, 95 – 102.

(21) Engstfeld, A. K.; Magaard, T.; Horch, S.; Chorkendorff, I.; Stephens, I. E. L. *Chemistry - A European Journal 0*.

(22) Hori, Y.; Murata, A.; Takahashi, R. *Journal of the Chemical Society, Faraday Transactions* **1989**, *85*, 2309–2326.

(23) Bagger, A.; Ju, W.; Varela, A. S.; Strasser, P.; Rossmeisl, J. *ChemPhysChem* **2017**, *18*, 3266–3273.

(24) Schouten, K. J. P.; Qin, Z.; Gallent, E. P.; Koper, M. T. M. *Journal of the American Chemical Society* **2012**, *134*, 9864–9867.

(25) Bagger, A.; Arnarson, L.; Hansen, M. H.; Spohr, E.; Rossmeisl, J. *Journal of the American Chemical Society* **2019**, *141*, 1506–1514.

(26) Ooka, H.; Figueiredo, M. C.; Koper, M. T. M. *Langmuir* **2017**, *33*, 9307–9313.

(27) Singh, M. R.; Kwon, Y.; Lum, Y.; Ager, J. W.; Bell, A. T. *Journal of the American Chemical Society* **2016**, *138*, 13006–13012, PMID: 27626299.

(28) Hori, Y.; Takahashi, I.; Koga, O.; Hoshi, N. *Journal of Molecular Catalysis A: Chemical* **2003**, *199*, 39 – 47, Special Issue dedicated to Professor Juro Horiuti in commemoration of his centennial birthday and his contribution to science.

(29) Matsushima, H.; Taranovskyy, A.; Haak, C.; Gründer, Y.; Magnussen, O. M. *Journal of the American Chemical Society* **2009**, *131*, 10362–10363.

(30) Inukai, J.; Osawa, Y.; Itaya, K. *The Journal of Physical Chemistry B* **1998**, *102*, 10034–10040.

(31) Bae, S.-E.; Gewirth, A. A. *Langmuir* **2006**, *22*, 10315–10321.

(32) Vogt, M.; Lachenwitzer, A.; Magnussen, O.; Behm, R. *Surface Science* **1998**, *399*, 49 – 69.

(33) Beverskog, B.; Puigdomenech, I. *Journal of The Electrochemical Society* **1997**, *144*.

(34) Herron, J. A.; Morikawa, Y.; Mavrikakis, M. *Proceedings of the National Academy of Sciences* **2016**, *113*, E4937–E4945.

(35) Naderian, M.; Groß, A. *The Journal of Chemical Physics* **2016**, *145*, 094703.

(36) Rossmeisl, J.; Chan, K.; Ahmed, R.; Tripkovic, V.; Bjørketun, M. E. *Phys. Chem. Chem. Phys.* **2013**, *15*, 10321–10325.

(37) H. Hansen, M.; Rossmeisl, J. *The Journal of Physical Chemistry C* **2016**, *120*, 29135–29143.

(38) Gossenberger, F.; Roman, T.; Groß, A. *Electrochimica Acta* **2016**, *216*, 152 – 159.

(39) Gossenberger, F.; Roman, T.; Groß, A. *Surface Science* **2015**, *631*, 17 – 22, Surface Science and Electrochemistry - 20 years later.

(40) Hansen, M. H.; Nilsson, A.; Rossmeisl, J. *Phys. Chem. Chem. Phys.* **2017**, *19*, 23505–23514.

(41) Katayama, Y.; Nattino, F.; Giordano, L.; Hwang, J.; Rao, R. R.; Andreussi, O.; Marzari, N.; Shao-Horn, Y. *The Journal of Physical Chemistry C* **2019**, *123*, 5951–5963.

(42) Kim, Y.-G.; Baricuatro, J. H.; Javier, A.; Gregoire, J. M.; Soriaga, M. P. *Langmuir* **2014**, *30*, 15053–15056.

 (2) Nørskov, J. K.; Rossmeisl, J.; Logadottir, A.; Lindqvist, L.; Kitchin, J. R.; Bligaard, T.; Jónsson, H. *The Journal of Physical Chemistry B* **2004**, *108*, 17886–17892.

(44) Trasatti, S. *Journal of Electroanalytical Chemistry and Interfacial Electrochemistry* **1986**, *209*, 417 – 428.

(45) Larsen, A. H. et al. *Journal of Physics: Condensed Matter* **2017**, *29*, 273002.

(46) Enkovaara, J. et al. *Journal of Physics: Condensed Matter* **2010**, *22*, 253202.

(47) Hammer, B.; Hansen, L. B.; Nørskov, J. K. *Phys. Rev. B* **1999**, *59*, 7413–7421.

(48) Berendsen, H. J. C.; Postma, J. P. M.; van Gunsteren, W. F.; DiNola, A.; Haak, J. R. *The Journal of Chemical Physics* **1984**, *81*, 3684–3690.
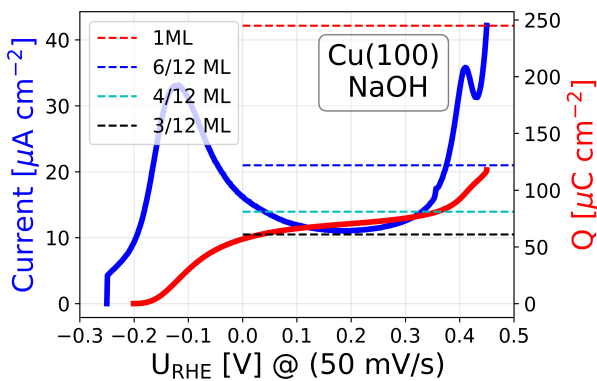
Supporting Information

<center>

Ab Initio Cyclic Voltammetry on

Cu(111), Cu(100) and Cu(110) in
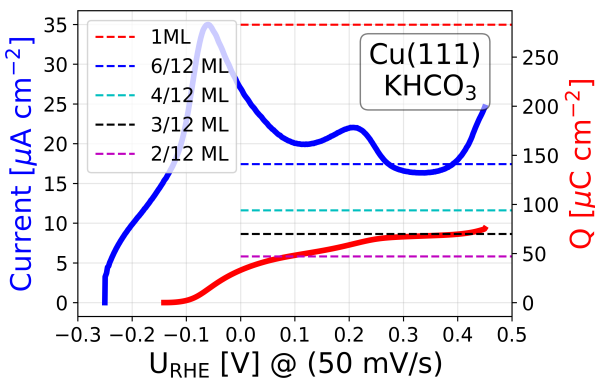
Acidic, Neutral and Alkaline

</center>

Alexander Bagger, Rosa M. Arán-Ais, Joakim Halldin Stenlid, Egon Campos dos Santos,

Logi Arnarson, Kim Degn Jensen, María Escudero-Escribano, B. Roldan Cuenya and Jan
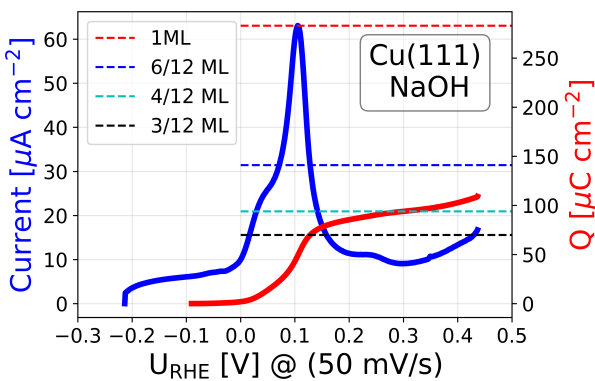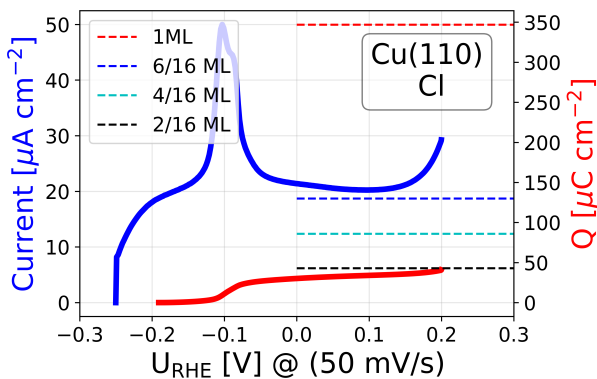
Rossmeisl

Figure S1: Shows the anodic CV (blue) and the integration (red) of anodic CV scans on relevant Cu facets and electrolytes. The integration can be compared to charges lines for each facet obtained as the charge of 1ML correspond to $283\mu C/cm^2$, $245\mu C/cm^2$ and $347\mu C/cm^2$ for Cu(111), Cu(100) and Cu(110), respectively. For Cu(110) having rows of atoms, both the top and bottom rows have been used to describe 1ML, given the highest charge pr cm^2.
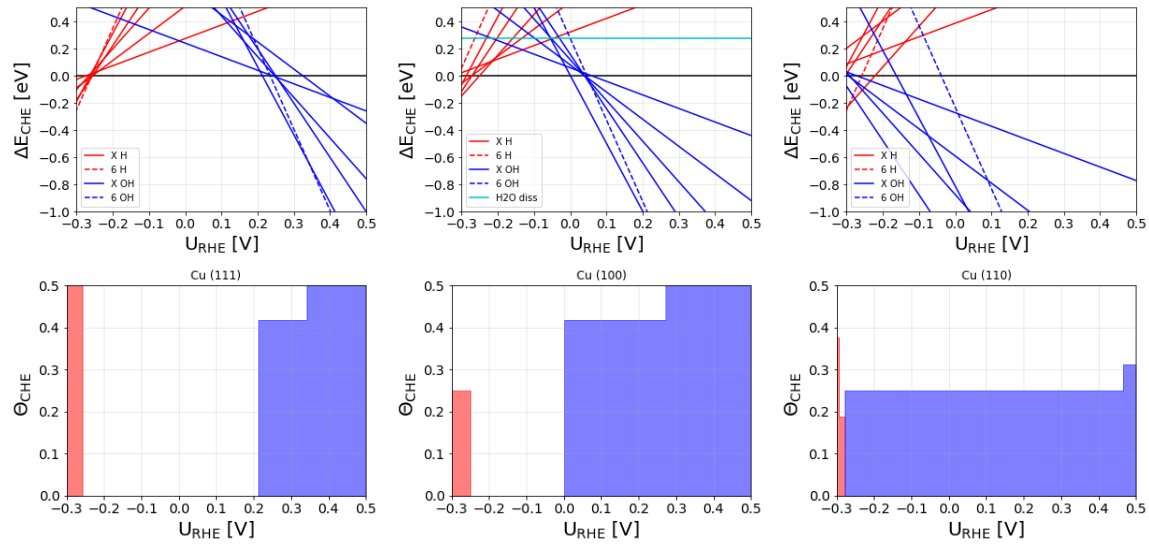
Figure S2: Vacuum binding energies and utilization of the CHE to create surface pourbaix diagram and coverages as a function of potential. H* and OH* structures from the AIMD simulations is used without the water.

Figure S3: Vacuum binding energies and utilization of the CHE to create surface pourbaix diagram and coverages as a function of potential. H*, OH*, HCO$_3^*$ and CO$_3$ structures from the AIMD simulations is used without the water. Note that HCO$_3^*$ and CO$_3$ structures are included, they are just so unstable that they are not visible.
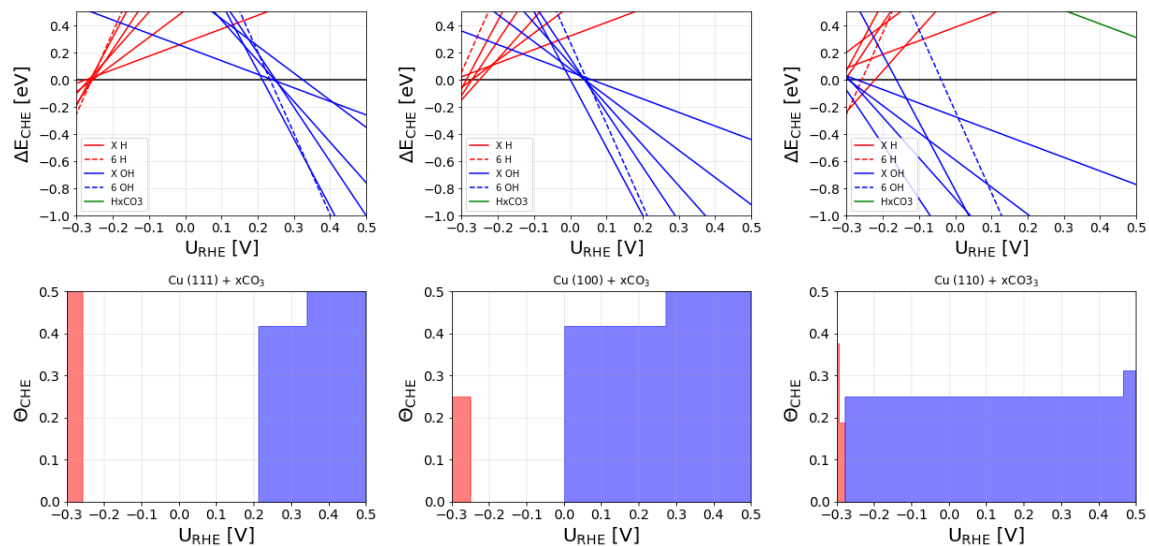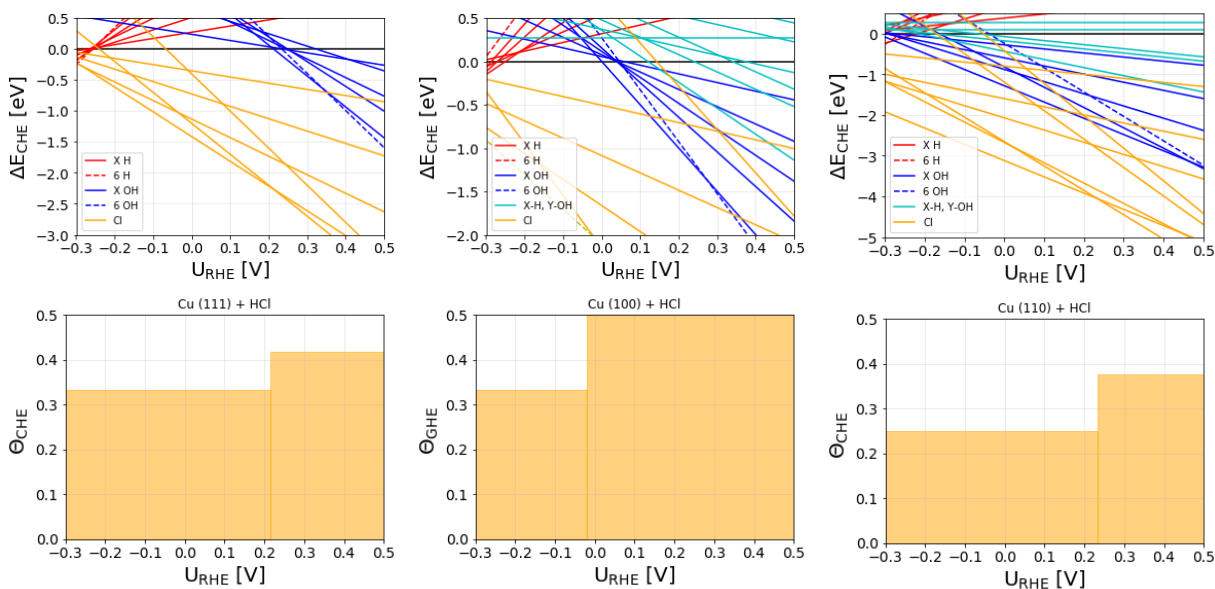
Figure S4: Vacuum binding energies and utilization of the CHE to create surface pourbaix diagram and coverages as a function of potential. H*, OH* and Cl* structures from the AIMD simulations is used without the water.
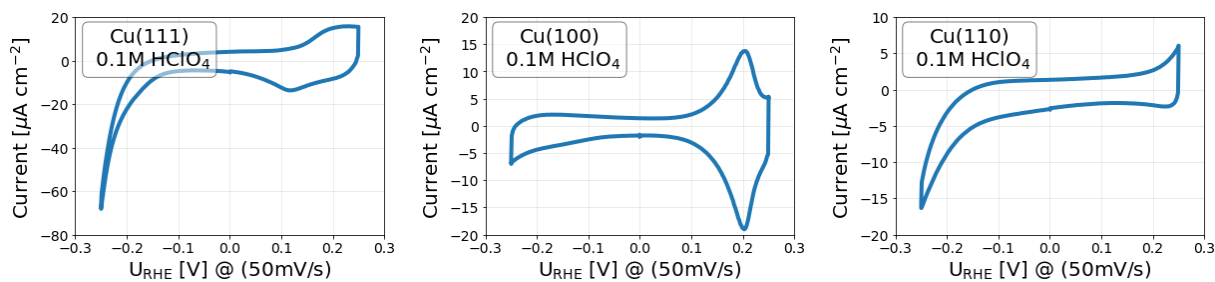

Figure S5: Experimental CVs in $HClO_4$ solutions on Cu(111), Cu(100) and Cu(110).

Table S1: Thermodynamic data used from Atkins[1] to set the energy of $Cl^-(aq)$ with respect to $Cl_2(g)$.

	1/2 $Cl_2(g)$	$\rightarrow$	$Cl^-(aq)$
ΔG	1/2 * 0 kJ/mol		-131.23 kJ/mol
			-1.36eV

Table S2: Thermodynamic data used from Atkins[1] to set the energy of Cl^* with respect to $Cl_2(g)$. We assume that at the surface the chlorine has zero entropy.

	1/2 $Cl_2(g)$	$\rightarrow$	Cl^*
-TΔS	-1/2*0.69 eV		0 eV
ZPE	0.049 eV		0.021 eV
ΔG$_2$			**0.317 eV**

Table S3: Thermodynamic data used for carbonate at 1M and pH=0.

	$H_2CO_3(aq)$	$HCO_3^-(aq)$	$CO_3^{2-}(aq)$
G [kJ/mol]	-623.08 kJ/mol	-586.77 kJ/mol	-527.81 kJ/mol

When including dissolved CO2(aq):

$$\frac{[H^+][HCO_3^-]}{[H_2CO_3]} = 4.4 \times 10^{-7}, \quad \frac{[H^+][CO_3^{2-}]}{[HCO_3^-]} = 4.69 \times 10^{-11}$$

At all pH

$$G_{H_2CO_3} = G_{HCO_3^- + H^+} = G_{CO_3^{2-} + 2H^+}$$

Hence at pH=8.3 and 0.1M, assuming majority of HCO_3^- and H_2CO_3

$$4.4 \times 10^{-7} = \frac{[H^+][HCO_3^-]}{[H_2CO_3]} = \frac{10^{-8.3} \times x}{0.1 - x} \leftrightarrow x = 0.09887$$

$$G_{HCO_3^- + H^+} = -586.77\text{kJ/mol} + k_B Tln([0.09887]) + k_B Tln([10^{-8.3}]) = -640.21\text{kJ/mol}$$

Table S4: Thermodynamic data used from Atkins[1] to set the energy of H_2CO_3 with respect to CO(g), H_2O(g) and H_2(g).

	CO(g)	+	2 * H_2O(g)	→	H_2CO_3 (aq)	+	H_2(g)
ΔG	-137.17 kJ/mol		-2 * 228.57 kJ/mol		-640.21 kJ/mol		0 kJ/mol
ΔG$_1$							**-0.48 eV**

Table S5: Thermodynamic data used from Atkins[1] and Nørskov et. al.[2] to set the energy of HCO_3^* and CO_3^* with respect to $CO(g)$, $H_2O(g)$ and $H_2(g)$. We assume that at the surface the carbonate has zero entropy.

	CO(g)	+	2 * H$_2$O(g)	→	HCO$_3^*$	+	3/2 H$_2$(g)	
-TΔS	-0.612 eV		-2 * 0.67 eV		0 eV		-3/2* 0.41 eV	
ZPE	0.13 eV		2 * 0.56 eV		0.728 eV		3/2 * 0.27 eV	
ΔG$_2$								**1.22 eV**

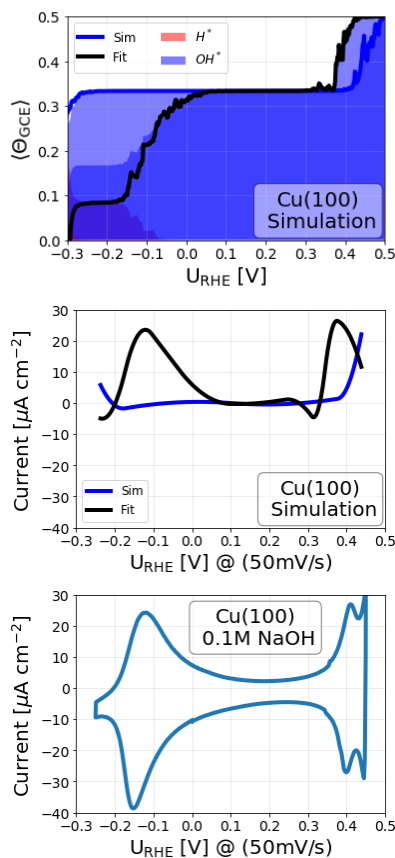|	CO(g)	+	2 * H$_2$O(g)	→	CO$_3^*$	+	2 H$_2$(g)	
-TΔS	-0.612 eV		-2 * 0.67 eV		0 eV		-2 0.41 eV	
ZPE	0.13 eV		2 * 0.56 eV		0.425 eV		2 * 0.27 eV	
ΔG$_2$								**0.85 eV**

Figure S6: Simulations and fitting of H* and OH* coverages including combinations for alkaline (NaOH) for the Cu(100) facet. Fitting parameters are given in Table S8.

Table S6: Fitting parameters obtained from fitting AIMD states to experimental NaOH CVs for Cu(111) and Cu(100).

Cu(111) NaOH	ΔE [eV]	Cu(100) NaOH	ΔE [eV]
$E(-1, p, \phi_{e^-})$	-0.072	$E(-1, p, \phi_{e^-})$	0.077
$E(-2, p, \phi_{e^-})$	0.192	$E(-2, p, \phi_{e^-})$	27.98
$E(-3, p, \phi_{e^-})$	0.243	$E(-3, p, \phi_{e^-})$	0.781
$E(-4, p, \phi_{e^-})$	0.402	$E(-4, p, \phi_{e^-})$	1.135
$E(-5, p, \phi_{e^-})$	8.264	$E(-5, p, \phi_{e^-})$	31.21
$E(-6, p, \phi_{e^-})$	0.594	$E(-6, p, \phi_{e^-})$	1.00
$E(n = \{1, .., 6\}, p, \phi_{e^-})$	0.080	$E(n = \{1, .., 6\}, p, \phi_{e^-})$	32.72

Table S7: Fitting parameters obtained from fitting AIMD states to experimental KHCO$_3$ CV for Cu(111). Left show prior with NaOH fitting parameters and right shows after fitting the CV.

Cu(111) KCO$_3$	ΔE [eV]	Cu(111) KCO$_3$	ΔE [eV]
$E(-1, p, \phi_{e^-})$	-0.072	$E(-1, p, \phi_{e^-})$	0.23
$E(-2, p, \phi_{e^-})$	0.192	$E(-2, p, \phi_{e^-})$	63.3
$E(-3, p, \phi_{e^-})$	0.243	$E(-3, p, \phi_{e^-})$	63.3
$E(-4, p, \phi_{e^-})$	0.402	$E(-4, p, \phi_{e^-})$	63.5
$E(-5, p, \phi_{e^-})$	8.264	$E(-5, p, \phi_{e^-})$	71.4
$E(-6, p, \phi_{e^-})$	0.594	$E(-6, p, \phi_{e^-})$	63.7
$E(n = \{1, .., 6\}, p, \phi_{e^-})$	0.080	$E(n = \{1, .., 6\}, p, \phi_{e^-})$	55.3
$E(\{1, 2, 3\}HCO3, p, \phi_{e^-})$	0.0	$E(\{1, 2, 3\}HCO3, p, \phi_{e^-})$	63.1
$E(CO3, p, \phi_{e^-})$	0.0	$E(CO3, p, \phi_{e^-})$	0.19
$E(2CO3, p, \phi_{e^-})$	0.0	$E(2CO3, p, \phi_{e^-})$	52.9

Table S8: Cu(100) fitting parameters for combinations of OH* and H* obtained from fitting AIMD states to experimental CV.

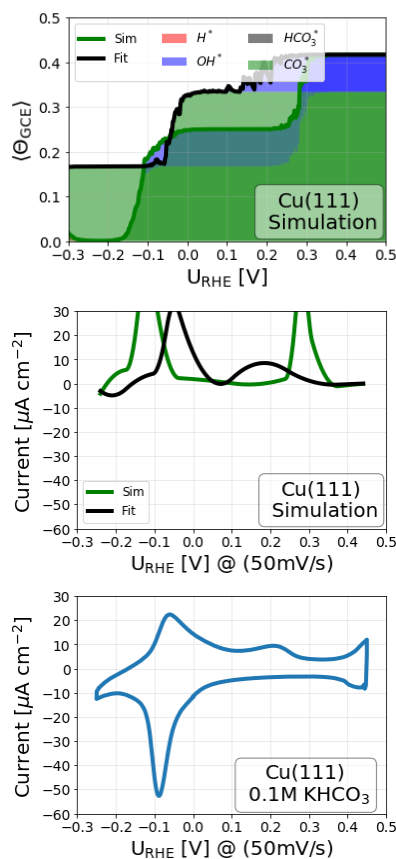| Cu(100) NaOH	ΔE [eV]
$E(-1, p, \phi_{e^-})$	0.195
$E(-2, p, \phi_{e^-})$	0.115
$E(-3, p, \phi_{e^-})$	0.310
$E(-4, p, \phi_{e^-})$	0.642
$E(-5, p, \phi_{e^-})$	10.95
$E(-6, p, \phi_{e^-})$	0.514
$E(n = \{1, .., 6\}, p, \phi_{e^-})$	-0.100

Figure S7: Simulations and fitting of stronger binding CO_3^* coverages for the Cu(111) facet in bicarbonate solution. Fitting parameters are given in Table S9.

Table S9: Fitting parameters obtained from fitting AIMD states to experimental $KHCO_3$ CV for Cu(111), when having a stronger binding of CO_3. These values are used in Figure S7.

Cu(111) KCO_3	ΔE [eV]
$E(-1, p, \phi_{e^-})$	0.21
$E(-2, p, \phi_{e^-})$	73.6
$E(-3, p, \phi_{e^-})$	73.7
$E(-4, p, \phi_{e^-})$	73.9
$E(-5, p, \phi_{e^-})$	81.7
$E(-6, p, \phi_{e^-})$	74.1
$E(n = \{1, .., 6\}, p, \phi_{e^-})$	65.7
$E(\{1, 2, 3\}HCO3, p, \phi_{e^-})$	73.5
$E(CO3, p, \phi_{e^-})$	-0.52
$E(2CO3, p, \phi_{e^-})$	-1.19

References

(1) Atkins, P. and Atkins, P.W. and de Paula, J., *Atkins' Physical Chemistry*, **2014**.

(2) Nørskov, J. K. and Rossmeisl, J. and Logadottir, A. and Lindqvist, L. and Kitchin, J. R. and Bligaard, T. and Jónsson, H., *The Journal of Physical Chemistry B*, **2004**,*108*, 17886-17892